Available online at www.sciencedirect.com

ScienceDirect

Advances in Space Research 77 (2026) 1304–1320

ADVANCES IN SPACE RESEARCH (a COSPAR publication)

www.elsevier.com/locate/asr

Superposed epoch analysis of solar energetic particle events observed in solar cycle 25

G.U. Farwa [a,*], N. Dresing [a], L. Vuorinen [a,b], C. Palmroos [a], J. Gieseler [a], R. Vainio [a]

[a] Department of Physics and Astronomy, University of Turku, Turku FI-20014, Finland
[b] Department of Physics and Astronomy, Queen Mary University of London, London E1 4NS, UK

Received 12 May 2025; received in revised form 24 October 2025; accepted 27 October 2025
Available online 4 November 2025

Abstract

Intensity-time profiles of solar energetic particles (SEPs) emitted during solar eruptions are shaped by a number of entangled processes. This involves the location of the particle source with respect to the observer, the type, location, and duration of the acceleration process, as well as potentially varying transport effects from the Sun to the observer. Understanding the behavior of these profiles can bring us closer to more reliable space weather forecasting. Using multi-spacecraft observations of SEP events of the early solar cycle 25, we aim to characterize an average SEP profile of the sample. We analyzed 45 SEP events from November 2020–May 2023 provided by the SERPENTINE multi-spacecraft SEP event catalog for ∼100-keV and ∼1-MeV electrons and 25–40 MeV protons, including observations by Solar Orbiter, STEREO A, BepiColombo, Parker Solar Probe, and near-Earth spacecraft (SOHO and Wind), resulting in more than 100 single spacecraft observations. We performed a superposed epoch analysis of the intensity-time profiles, normalized with peak intensity and rise time, separating the events into magnetically well-connected and poorly-connected sectors from the source at the Sun. We also consider the rise and the decay phases separately. We studied the behavior of the mean curves and applied empirical exponential and power law models to fit the mean profiles. We also studied the onset delay between relativistic electrons and protons to validate the potential application of the early arrival of relativistic electrons to forecast the hazardous energetic protons. We find that although the sample contains both impulsive and gradual profiles, they seem to follow the same trend when normalized and are, mostly, better represented by the power law and sometimes by the exponential law. Furthermore, the normalized mean curves for electron and proton profiles do not differ significantly from each other. We conclude that despite having a mixture of impulsive and gradual profiles in the sample, and potentially different contributions from flare and shock acceleration, a representative average SEP profile can be determined. The similarity of the mean normalized SEP profiles of high-energy electrons and protons supports the use of the early alert of relativistic electrons to forecast the later-arriving energetic protons and suggests that the forecasting scheme should work better with high-energy electrons.

Keywords: Sun; Solar energetic particles; Acceleration; Intensity profile; Solar flare

1. Introduction

Solar energetic particles (SEPs) are charged particles emitted from the Sun during solar eruptions such as solar flares and fast coronal mass ejections (CMEs) (Reames, 2015). SEP events consist of energetic electrons, protons, and heavier ions, typically with energies ranging from a few tens of keV to a few tens of MeV, reaching up to GeV in the case of major SEP events (Vainio et al., 2009). Large SEP events can cause solar radiation storms having a direct space weather impact on the electronics of space vehicles and satellites (Iucci et al., 2005), distorting radio communications (Fiori et al., 2022), and presenting a

* Corresponding author.
E-mail address: ghulam.u.farwa@utu.fi (G.U. Farwa).

https://doi.org/10.1016/j.asr.2025.10.099
0273-1177/

radiation hazard to humans in space and aircrew in the upper atmosphere (Getley et al., 2005; Beck et al., 2005).

Intensity profiles of SEP events can exhibit different shapes for different particle species, energies, and observer locations. Both source and transport effects influence the characteristics of SEP observations, implying that SEP intensity profiles contain significant information about the origin, acceleration, and transport processes of SEPs. The profiles have been found to show a certain organization concerning the helio-longitudinal location of the observer from the source region (Reames et al., 1996; Dresing et al., 2014; Cane et al., 1988; Cane, 1985; Kecskeméty et al., 2009; Richardson et al., 2014). Wang et al. (2022) concluded that the location of the observer, along with the SEP transport conditions, plays an important role in characterizing the intensity-time profiles of SEPs. Cane et al. (1988) reported that in shock-associated events, the respective position of the observer to the shock front leads to very different time profiles because the magnetic connection to the source region changes when the CME propagates further away from the Sun.

According to the historical description presented by Reames (1999), SEP events are roughly classified into impulsive and gradual events. Impulsive SEP events are characterized by a fast-rising profile and higher electron-to-proton ratios. They are mostly associated with impulsive flares and only narrow CMEs, and they are assumed to be accelerated by processes related to the flare. In contrast, gradual SEP events are characterized by slow-rising and long-lasting intensity profiles and are believed to be mainly accelerated by shocks driven by fast and wide CMEs (Cane et al., 1988). Results by Lario (2010) and Wang et al. (2021) also support the contribution of interplanetary shocks toward the slow and prolonged rise in SEP intensities.

Hence, studying the shapes of SEP intensity-time profiles could unveil the relative contribution of solar flares and CME-driven shocks towards particle acceleration. However, SEP transport processes from the corona through the interplanetary (IP) medium to Earth have been found to alter SEP characteristics and can potentially strongly vary from event to event (Haggerty and Roelof, 2002; Haggerty et al., 2003; Krucker et al., 2007; Lario et al., 2013; Rodríguez-García et al., 2023). Disentangling source and transport mechanisms is still challenging in current SEP research. Being able to make good predictions about SEP time profiles is, however, strongly desired to achieve more reliable space-weather forecasting against SEP radiation hazards.

The present study is an effort to characterize the intensity-time profiles of large SEP events using multi-spacecraft observations of ∼100-keV and ∼1-MeV electrons and >25-MeV protons from a sample of 45 SEP events that occurred in early solar cycle 25 between November 2020 and May 2023 (Dresing et al., 2024). The sample of 45 independent events observed by up to five different spacecraft results in more than 100 single spacecraft observations providing a data set of reasonable statistics of the latest solar cycle 25. We separate the events, similar to Farwa et al. (2025), into those that are magnetically well-connected and poorly-connected to the source region at the Sun. The average SEP event profile is examined using a superposed epoch analysis and fitted with different empirical functions. The resulting fits are compared among electrons and protons to investigate similarities and differences and to determine a characteristic SEP intensity-time profile.

In a recent study Farwa et al. (2025) analyzed the same sample of 45 multi-spacecraft SEP events used for the present study. The authors performed a correlation study of the peak intensities of ∼100-keV and ∼1-MeV electrons with those of >25-MeV protons for magnetically well-connected and poorly-connected events. Farwa et al. (2025) proposed that the well-connected events contain a mixture of flare and CME-driven shock contribution, while the poorly-connected events are associated with the shock only.

Relativistic electrons, which have a propagation speed advantage over heavier ions, can be used as an early alert for the later-arriving energetic protons that pose radiation hazards to humans and technology. Posner (2007) demonstrated that the information carried by the relativistic electrons of a SEP event can be utilized to estimate the rise time and intensity of the upcoming energetic protons. The author applied the onset fitting analysis to the rise profiles of electrons and protons, with exponential fits describing the steepest part of the rise. Based on this forecasting model, an average onset delay of one hour is reported for <50 MeV protons compared to the onset of relativistic electrons. Using the present event sample, we also analyze this warning time.

The structure of the paper is as follows: Section 2 introduces the datasets used in the analysis as well as the classification of events and analysis methods, Section 3 presents the results of the study, Section 4 provides the discussion of the results, and Section 5 summarizes the study.

2. Data selection and analysis

In this study, we investigate the intensity-time profiles of 45 multi-spacecraft SEP events observed between November 2020 and May 2023. The SEP events of this sample are reported for ∼25–40-MeV protons and ∼100-keV and ∼1-MeV electrons by Dresing et al. (2024) in the SERPENTINE multi-spacecraft SEP event catalog[1]. The SEP event selection criterion for the SERPENTINE catalog is that a proton event must be observed at 25–40 MeV by at least two spacecraft. The catalog includes data from multiple missions: Solar Orbiter (SolO; Müller et al., 2020), near-Earth spacecraft SOHO (Domingo et al., 1995) and Wind

[1] The latest version V3 of the catalog is available at https://data.serpentine-h2020.eu/catalogs/sep-sc25/ and athttps://zenodo.org/doi/10.5281/zenodo.10732268

(Ogilvie and Desch, 1997; Wilson et al., 2021), STEREO-A (Kaiser et al., 2008), BepiColombo (Benkhoff et al., 2021), and Parker Solar Probe (PSP; Fox et al., 2016). We note that the PSP electron data are so far only provided in count rates instead of intensities. For details of the instruments used for the observation of these SEP events, see Dresing et al. (2024) and Farwa et al. (2025). All of these 45 SEP events are reported to have an associated CME, while an associated flare could be identified for 40 events. The SEP observations of the sample are taken at different heliocentric radial distances (r) of the observing spacecraft varying from 0.07 to 1.01 au.

The SEP events of the sample are subdivided into well-connected, poorly-connected western, and poorly-connected eastern events based on the longitudinal separation angle between the associated flare and the observers' magnetic footpoint position at the Sun $\Delta\Phi = \Phi_{\text{flare}} - \Phi_{\text{SC}}$ (Lario et al., 2013), where Φ_{flare} is the longitude of the flare and Φ_{SC} is the longitude of the spacecraft magnetic footpoint. These angular parameters are calculated using the Solar-MACH tool (Gieseler et al., 2023), which relies on ballistic back-mapping. The solar wind speed used for the back-mapping is taken from measurements at each spacecraft at the time of the SEP onset and is provided in the SERPENTINE catalog. When solar wind measurements were unavailable at the spacecraft, a nominal value of 400 km/s was used. The SEP events with a longitudinal separation $-35^\circ \leqslant \Delta\Phi \leqslant 35^\circ$ are taken as well-connected to the source region. The SEP events with a longitudinal separation $35^\circ \leqslant \Delta\Phi \leqslant 180^\circ$ and $-180^\circ \leqslant \Delta\Phi \leqslant -35^\circ$ are taken as the poorly-connected western and the poorly-connected eastern events, respectively. For details, see Farwa et al. (2025).

Among the 45 SEP events of the sample, five events do not have information on the associated flare, leaving 40 events for the superposed epoch analysis, separated into the three longitudinal sectors. The background-subtracted intensity-time profiles of all 40 SEP events of the sample are analyzed for both the rise and the decay phases. The multi-spacecraft observations of the 40 independent SEP events resulted in 100, 83, and 110 single spacecraft observations for ~100-keV, ~1-MeV electrons, and ~25–40-MeV protons, respectively. In case of SEP events with successive bursts of SEPs due to ongoing solar activity, there can be additional peaks during the decay phase of the analyzed event. In such cases, we limited the selection of the SEP events to those profiles showing only one peak in SEP intensity time profile to avoid the mixing of events from overlapping successive activity.

While considering the cruising speed of PSP at smaller heliocentric distances, one PSP profile measured at $r = 0.07$au is excluded from the decay profiles. Here we noticed a prominent changing magnetic connection (34°) from the source throughout the event, i.e., from the onset to the decay of the profile.

Measurements of near-relativistic ~100-keV electrons made with single-detector instruments, based on the measurement of electrons using a foil to stop the ions from entering the detector, may suffer from contamination by ions energetic enough to just pass the foil or by more energetic ions penetrating the passive collimator of the instrument. This occurs mainly when ion fluxes are large compared to the electron fluxes (e.g., Wraase et al., 2018; Kartavykh et al., 2025). These contamination effects become more prominent during SEP peak phases than during SEP onsets due to the usually later arrival times of ions. Therefore, we checked all 100 observations for ~100-keV electrons by comparing the electron intensity-time profiles with those of ions in the contaminating energy ranges and excluded the 36 single spacecraft observations where we found potential contamination by ions, leaving 64 observations included in the decay-phase analysis for ~100-keV electrons.

We further note that we have excluded all SOHO/EPHIN observations of ~1-MeV electrons from this study due to potential ion contamination recently identified by the instrument team (private communication, B. Heber, University of Kiel, Germany). This further reduces the ~1-MeV electron single-spacecraft observations from 83 to 59.

We also noticed some events with intensity-time series data missing after the peak and excluded such profiles from the superposed epoch analysis for the decay phase. In this way, we have excluded 20–30% of the single-spacecraft observations from the analysis for the decay phase, finally leaving 64, 48, and 74 single-spacecraft observations for ~100-keV, ~1-MeV electrons, and ~25–40-MeV protons, respectively. The details of the number of single-spacecraft observations used in different longitudinal sectors for both electron energies and protons are described in Table 1.

The normalized mean and the median profiles for ~100-keV, ~1-MeV electrons, and ~25–40-MeV protons are provided as CSV files as supplementary material to the study at Zenodo https://zenodo.org/records/16965300.

2.1. Analysis

Our study focuses on the average behavior of an SEP event determined from observations of multiple spacecraft at different heliocentric and helio-longitudinal locations. We applied a superposed epoch analysis to normalized intensity-time profiles of ~100-keV electrons, ~1-MeV electrons, and ⩾25-MeV protons for the well-connected and the poorly-connected western and the poorly-connected eastern events. Fig. 1 shows the superposed normalized intensity-time profiles of all SEP events of the sample used for this analysis for ~100-keV electrons (top), ~1-MeV electrons (center), and ⩾25-MeV protons (bottom) for three longitudinal sectors. Measurements along the negative x-axis represent the normalized background intensity level measured before the onset of an SEP event. The intensity along the y-axis is normalized to the peak intensity as $I_{\text{n}} = I/I_{\text{peak}}$ where I is the instantaneous intensity

Table 1
Number of single-spacecraft observations of the SEP events included in the superposed epoch analysis of the sample.

Event	~100-keV electrons	~1-MeV electrons	⩾25-MeV protons
Rise-phase			
Well-connected	42	22	42
Western	31	17	22
Eastern	27	20	36
Total	100	59	110
Decay-phase			
Well-connected	31	20	34
Western	24	14	19
Eastern	09	14	21
Total	64	48	74

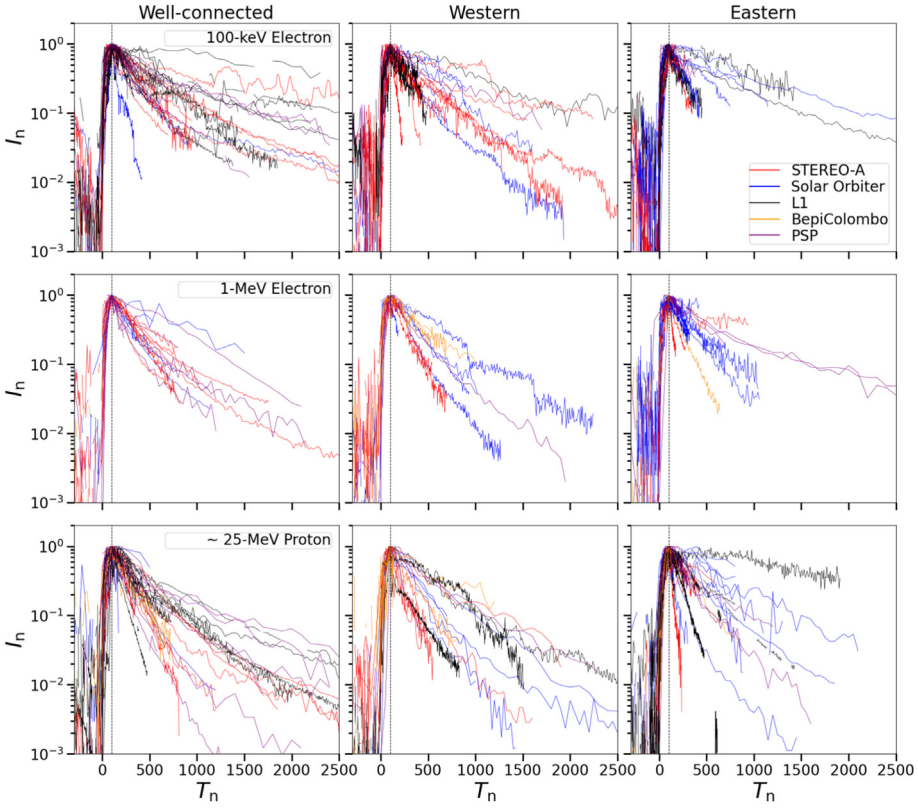

Fig. 1. Normalized intensity-time profiles of SEP events observed by multiple spacecraft for ~100-keV electrons (top row), ~1-MeV electrons (middle row), and ⩾25-MeV protons (bottom row) for well-connected (left), western (middle), and eastern (right) events. Normalized intensity and normalized time are plotted along the y- and x-axes, respectively. The black dotted vertical line at $T_n = 100$ represents the normalized peak time for all superposed profiles. The color scheme represents the corresponding spacecraft observations as listed in the legend.

and I_{peak} is the peak intensity of an observed SEP event. The time along the x-axis is normalized to the rise time of the SEP event as $T_n = 100\,(T - T_{onset})/(T_{peak} - T_{onset})$ where T_{onset} and T_{peak} are the onset and peak time of an SEP event, respectively, with $T_{peak} - T_{onset}$ defined as the "rise time". The shapes of superposed normalized profiles of all three particle types are studied and compared for the well-connected and the poorly-connected events.

We limit the analysis to the early decay interval of all SEP events, i.e., normalized times up to $T_n = 1000$ (10 times the rise time). Small data gaps of the order of a few tens of normalized time units appearing in some of the normalized intensity series in Fig. 1 are linearly interpolated to calculate the superposed epoch analysis parameters. The superposed epoch analysis results, including the mean and the median profiles, are calculated separately for the rise and decay phases. Fig. 2 shows the mean (green) and the median (lime) curves as well as the inter-quartiles (gray shaded regions) calculated for the rise phase of the superposed profiles of the well-connected SEP events. Fig. 3

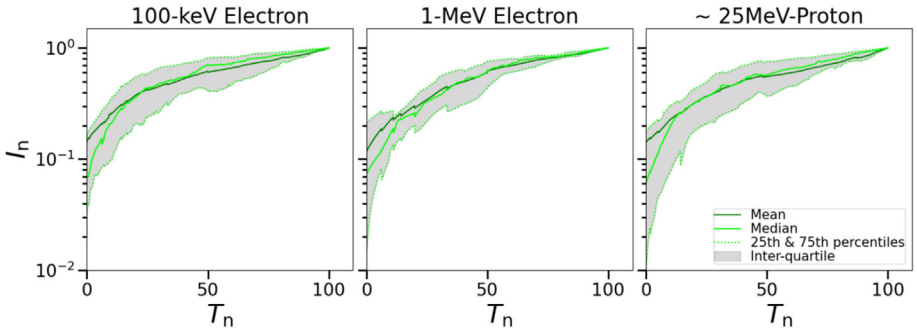

Fig. 2. The mean (green solid curve) and median (lime solid curve) calculated for the rise phase of superposed profiles of SEP events observed for ∼100-keV electrons (left), ∼1-MeV electrons (middle), and ⩾ 25-MeV protons (right) for well-connected events. The upper and lower lime-colored dotted curves represent the 25th and 75th percentiles of the superposed profiles. The inter-quartile region is shaded in gray. (For interpretation of the references to colour in this figure legend, the reader is referred to the web version of this article.)

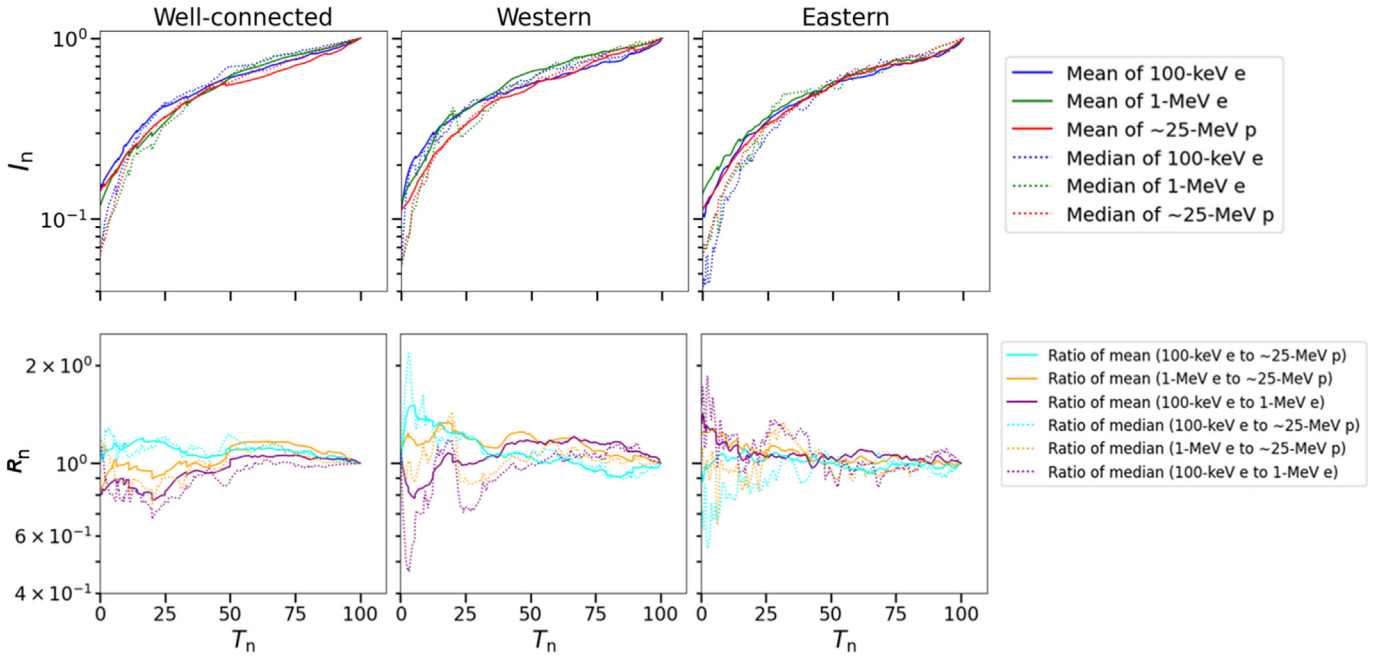

Fig. 3. The mean (solid curve) and median (dotted curve) (top panel) calculated for the rise phase of superposed profiles of SEP events observed for ∼100-keV electrons (blue), ∼1-MeV electrons (green), and ⩾ 25-MeV protons (red) for well-connected (left), western (middle), and eastern (right) events. The bottom panel shows the ratio R_n of the mean/ median (solid/ dotted curve) of the superposed normalized intensities for ∼100-keV electrons to ⩾25-MeV protons (cyan), ∼1-MeV electrons to ⩾25-MeV protons (orange), and ∼1-MeV electrons to ∼100-keV electrons (violet) for all three longitudinal sectors for the rise phase. (For interpretation of the references to colour in this figure legend, the reader is referred to the web version of this article.)

(top panel) summarizes all mean (solid) and the median (dotted) curves calculated for the rise phase of the superposed profiles of ∼100-keV electrons (blue), ∼1-MeV electrons (green), and ⩾25-MeV protons (red) separated by longitudinal sector. The ratio of the mean and the median, R_n, of the superposed normalized intensities is also calculated for all particle types of the sample and shown in Fig. 3 (bottom panel).

We also investigated the variation of the time normalization parameter, i.e., the rise time, among all three particle types of the sample (see D). The variation of intensity normalization parameter, i.e., peak intensity, has already been shown by (Farwa et al., 2025) (see their Fig. 2).

To characterize the average shape of an SEP event, we applied empirical models including an exponential law $I_n = e^{-(T_n-100)/b}$ and a power law $I_n = (T_n/100)^d$ to each mean curve. We note that these are single-parameter fits, i.e., the intercept is not a fitted variable but fixed to match the condition that $I_n = 1$ at $T_n = 100$. We calculated the fit parameters and reduced chi-squares for each fit, and details of these calculations for the three types of particles for all longitudinal sectors are provided in Table A.2 for both the rise and the decay phases. Fig. 4 shows the empirical models applied to the mean for the well-connected events. In blue and red, we show the fit of the exponential function and a power-law, respectively. The uncertainty in the mean

Table A.2
Fit parameters and values of reduced chi-squares calculated for exponential, power law, diffusion, and the Weibull model applied on the mean of superposed normalized intensity profiles of SEP events of the sample.

Event	Fit parameters				Reduced chi-square			
	Exp[a].	Pow[b].	Diffusion[c]	Weibull [d]	Exp[e].	Pow[f].	Diffusion[g]	Weibull[h]
				Rise-phase				
~100-keV electrons								
Well-connected	-7.79×10^{1} ±0.38%[i]	7.30×10^{-1} ±0.31%	1.42×10^{0} ±0.98%[j] 3.68×10^{0} ±25%[m]	1.40×10^{1}±9.30%[k] -8.90×10^{-1}±1.18%[n]	3.69×10^{0}	**1.80×10^{0}**[l]	3.02×10^{1}	7.96×10^{0}
Western	-7.43×10^{1} ±0.34%	7.83×10^{-1} ±0.63%	1.45×10^{0} ±0.94% 1.12×10^{0} ±87%	1.13×10^{0}±116.82% -0.78×10^{0}±1.38%	**2.02×10^{0}**	5.00×10^{0}	2.87×10^{1}	7.78×10^{0}
Eastern	-6.77×10^{1} ±0.40%	8.79×10^{-1} ±0.57%	0.91×10^{0} ±0.85% 16.51×10^{0} ±5.17%	3.57×10^{0}±12.87% -0.53×10^{0}±0.82%	**2.85×10^{0}**	4.25×10^{0}	2.57×10^{1}	1.02×10^{1}
~1-MeV electrons								
Well-connected	-8.16×10^{1} ±0.55%	7.62×10^{-1} ±0.15%	1.89×10^{0} ±0.76% 1.25×10^{0} ±63%	1.12×10^{1}±11.40% -1.07×10^{0}±1.08%	8.16×10^{0}	**4.39×10^{-1}**	2.40×10^{1}	4.76×10^{0}
Western	-9.90×10^{1} ±0.47%	6.53×10^{-1} ±0.19%	2.27×10^{0} ±0.62% -23.64×10^{0} ±3.19%	3.28×10^{1}±3.50% -1.19×10^{0}±0.83%	3.73×10^{0}	**4.85×10^{-1}**	1.80×10^{1}	2.21×10^{0}
Eastern	-7.70×10^{1} ±0.33%	8.08×10^{-1} ±0.46%	1.02×10^{0} ±0.45% 28.32×10^{0} ±2.50%	2.82×10^{0}±43.28% -0.87×10^{0}±1.26%	**1.85×10^{0}**	2.67×10^{0}	2.25×10^{1}	5.15×10^{0}
~25-MeV Protons								
Well-connected	-7.14×10^{1} ±0.48%	8.01×10^{-1} ±0.28%	2.07×10^{0} ±0.61% -6.94×10^{0} ±11.93%	2.72×10^{1}±4.93% -1.20×10^{0}±0.90%	**1.66×10^{0}**	3.79×10^{0}	3.03×10^{1}	5.30×10^{0}
Western	-6.75×10^{1} ±0.35%	8.13×10^{-1} ±0.32%	2.06×10^{0} ±0.63% -16.55×10^{0} ±5.03%	3.03×10^{1}±4.06% -1.15×10^{0}±0.96%	3.11×10^{0}	**1.79×10^{0}**	2.72×10^{1}	4.32×10^{0}
Eastern	-6.79×10^{1} ±0.36%	8.41×10^{-1} ±0.36%	1.70×10^{0} ±1.37% -8.25×10^{0} ±11.83%	1.74×10^{1}±8.48% -0.98×10^{0}±1.64%	**3.97×10^{0}**	4.17×10^{0}	3.56×10^{1}	7.76×10^{0}
				Decay-phase				
~100-keV electrons								
Well-connected	3.43×10^{2} ±0.45%	-7.01×10^{-1} ±0.16%	1.34×10^{0} ±0.94% 4.52×10^{0} ±20.10%	5.52×10^{1}±1.33% -1.13×10^{0}±0.98%	4.38×10^{0}	**7.34×10^{-1}**	3.81×10^{0}	9.00×10^{0}
Western	3.63×10^{2} ±0.62%	-7.04×10^{-1} ±0.14%	1.44×10^{0} ±0.94% 1.12×10^{0} ±86.91%	4.66×10^{1}±1.09% -0.74×10^{0}±0.53%	5.78×10^{0}	**3.61×10^{-1}**	4.73×10^{0}	5.36×10^{0}
Eastern	5.03×10^{2} ±0.67%	-5.82×10^{-1} ±0.36%	0.91×10^{0} ±0.85% 16.51×10^{0} ±5.17%	7.36×10^{1}±1.67% -0.57×10^{0}±0.64%	2.61×10^{0}	**9.28×10^{-1}**	2.53×10^{0}	2.84×10^{0}
~1-MeV electrons								
Well-connected	2.45×10^{2} ±0.32%	-9.18×10^{-1} ±0.29%	1.89×10^{0} ±0.75% 3.84×10^{0} ±19.91%	8.38×10^{1}±1.22% -1.65×10^{0}±0.94%	**2.33×10^{0}**	2.98×10^{0}	2.34×10^{0}	6.10×10^{0}
Western	2.75×10^{2} ±0.24%	-9.31×10^{-1} ±0.40%	2.34×10^{0} ±0.60% -28.39×10^{0} ±2.53%	7.80×10^{1}±1.62% -0.96×10^{0}±0.18%	**1.02×10^{0}**	4.48×10^{0}	7.67×10^{-1}	0.80×10^{0}
Eastern	3.09×10^{2} ±0.44%	-8.34×10^{-1} ±0.21%	1.00×10^{0} ±0.49% 31.22×10^{0} ±2.41%	8.12×10^{1}±1.74% -0.86×10^{0}±0.35%	2.13×10^{0}	**6.92×10^{-1}**	1.63×10^{0}	1.80×10^{0}
~25-MeV Protons								
Well-connected	2.62×10^{2} ±0.25%	-1.03×10^{0} ±0.27%	2.13×10^{0} ±0.56% -12.53×10^{0} ±6.39%	6.72×10^{1}±2.33% -1.00×10^{0}±0.17%	**3.08×10^{0}**	5.00×10^{0}	1.72×10^{0}	1.71×10^{0}

(*continued on next page*)

Table A.2 (*continued*)

Event	Fit parameters			Reduced chi-square			
	Exp[a].	Pow[b].	Diffusion[c]	Weibull[d]	Exp[e].	Pow[f].	Diffusion[g]	Weibull[h]
Western	2.81×10^{2} ±0.38%	-9.58×10^{-1} ±0.15%	2.14×10^{0} ±0.57% -24.82×10^{0} ±3.08%	8.92×10^{1}±2.02% -0.94×10^{0}±0.27%	2.75×10^{0}	**5.69×10^{-1}**	1.60×10^{0}	1.67×10^{0}
Eastern	2.94×10^{2} ±0.64%	-8.02×10^{-1} ±0.21%	1.75×10^{0} ±1.23% -12.31×10^{0} ±8.50%	7.12×10^{1}±1.49% -0.74×10^{0}±0.53%	2.79×10^{0}	**4.04×10^{-1}**	2.84×10^{0}	5.36×10^{0}

[a] Fit parameters calculated for exponential,
[b] power law,
[c] diffusion model
[d] Weibull model.
[e] Values of reduced chi-squares calculated for exponential,
[f] power law,
[g] diffusion model,
[h] Weibull model.
[i] Percentage error in the value of the fit parameter.
[j] The value of fit parameter *c* for the diffusion model.
[k] The value of fit parameter *l* for the Weibull model.
[l] The lower value of reduced chi-square, among exponential and power law fits, highlighted in boldface to represent the better fit.
[m] The value of fit parameter *a* for the diffusion model.
[n] The value of fit parameter *m* for the Weibull model.

(μ, purple shaded area) is calculated as $\mu \pm \sigma$, where σ is the standard error of the mean calculated from superposed epoch analysis. The values of the reduced chi-squares calculated for both the exponential and the power law fits are provided in the figure legends.

Similarly, we calculated and compared the superposed epoch analysis parameters for the decay phases of the normalized intensity profiles of the sample. Fig. 5 shows the mean, the median, and the inter-quartiles calculated for the decay phase of intensity profiles of SEP events in the well-connected events.

Fig. 6 compares the mean (solid) and the median (dotted) curves calculated for the decay phase of the superposed normalized intensity profiles for three longitudinal sectors.

The ratio of the mean and the median, R_n, of the superposed normalized intensities is calculated for all particle types for the decay phase sample as well (Fig. 6, bottom panel).

Fig. 7 shows two empirical models applied to fit the mean (black solid) curves of the decay phases in the well-connected events.

3. Results

3.1. Superposed epoch analysis

Comparing the normalized intensity profiles of the sample (Fig. 1), we notice that the profiles contain a large variety of decay profiles in all longitudinal sectors. A larger variation in the decay profiles is expected due to the normalization with respect to the rise times.

The superposed epoch analysis of the rise times yields rather similar shapes for the mean curves (Fig. 3), when comparing the different particle types, which is also reflected in the ratios shown in the bottom panel of the figure. The same is true for the median curves in all three longitudinal sectors. In the case of the mean decay profiles, we find that $\geqslant$25-MeV protons and ~1-MeV electrons show a rather similar behavior while the ~100-keV electrons deviate more strongly (Fig. 6, top panel).

The ratio of the mean (median) electron to mean (median) proton profiles (bottom panels of Figs. 3 and 6) supports the similarity in $\geqslant$25-MeV protons and ~1-MeV electrons average profile behavior.

We notice that for all three particle types, both exponential and power law models applied on decay profiles are rather similar until normalized times of about 500 (Fig. 7), after which the two models deviate strongly.

3.2. Comparison of empirical models

To determine which fit best describes the mean profiles for both the rise and decay phases, we compared the values of reduced chi-squares for exponential and power law model (Table A.2) calculated for all particle types in all longitudinal sectors, and the fit with the lower value of

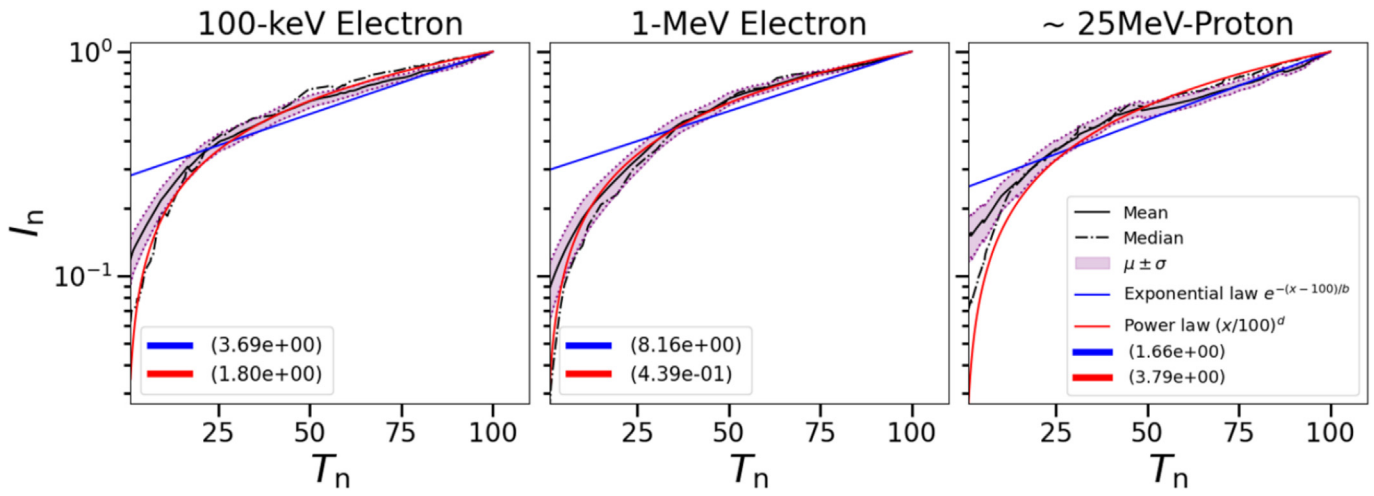

Fig. 4. An exponential (blue curve) and power (red curve) law fit applied on the mean (black solid curve) calculated for the rise phase of superposed profiles of SEP events observed for ~100-keV electrons (left), ~1-MeV electrons (middle), and ⩾ 25-MeV protons (right) for well-connected events. The purple-shaded region represents the uncertainty in the mean (μ) calculated as $\mu \pm \sigma$, where σ is the standard error of the mean. The value of the reduced chi-square calculated for both exponential (blue) and power (red) law fits is listed in the legend box in the corresponding color. (For interpretation of the references to colour in this figure legend, the reader is referred to the web version of this article.)

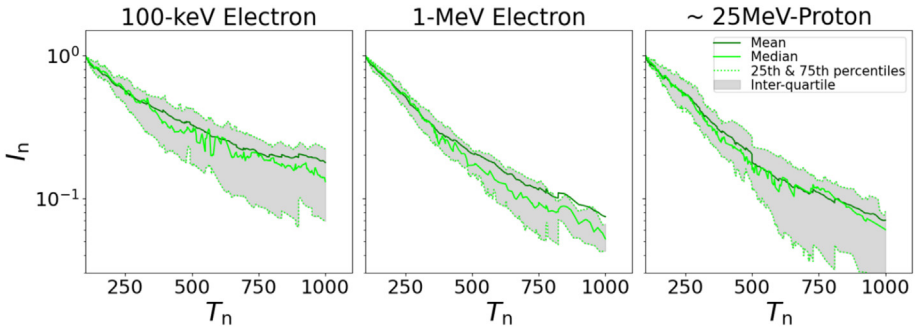

Fig. 5. The mean (solid green curve) and median (solid lime curve) calculated for the decay phase of superposed profiles of SEP events observed for ~100-keV electrons (left), ~1-MeV electrons (middle), and ⩾25-MeV protons (right) for well-connected events. The upper and lower lime-colored dotted curves represent the 25th and 75th percentiles of the superposed profiles. The inter-quartile region is shaded as gray. (For interpretation of the references to colour in this figure legend, the reader is referred to the web version of this article.)

reduced chi-square is considered as the better fit. Fig. 8 shows the fit results of the exponential (dashed-dotted curves) and power law (solid curves) models applied for both the rise (upper panel) and the decay (lower panel) phases for all particle types in all longitudinal sectors, highlighting the better fit in brighter and thicker curves. For both the rise and the decay profiles, we note that none of the exponential or power law models always represent the mean behavior better than the other. For the case of the rise phase, the mean behavior of five (four) profiles is better represented by the exponential (power law) model. The resulting fits of each individual model are often very similar along the different particle types. Especially in the rise profiles of the poorly-connected eastern events, where the exponential law is always found to be the better model, the profiles for ~100-keV electrons and ⩾25-MeV protons are precisely aligned. The well-connected rise profiles (Fig. 8, top left) better represented by a power law for ~100-keV and ~1-MeV electrons are also very similarly aligned together. In the case of the decay phases, the mean behavior is most often better represented by a power law as compared to the exponential law (six out of nine profiles). We note that the mean decay profiles for ~1-MeV electrons and ⩾25-MeV protons are quite similar in the well-connected and especially for the poorly-connected eastern events (Fig. 8).

Fig. 9 summarizes the results of our analysis by presenting all the superposed epoch analysis parameters together for both the rise and the decay phases of the SEP events. We note that the scaling of the time axis (x-axis) is different for the rise and the decay phase (i.e., left and right of the vertical line). The fits of the empirical models of the exponential and power law as shown in Fig. 8 are also included. The results are also compared with a diffusion model 1, green curve, obtained from the diffusion function model of Wang et al. (2022) by requiring the profile to start at

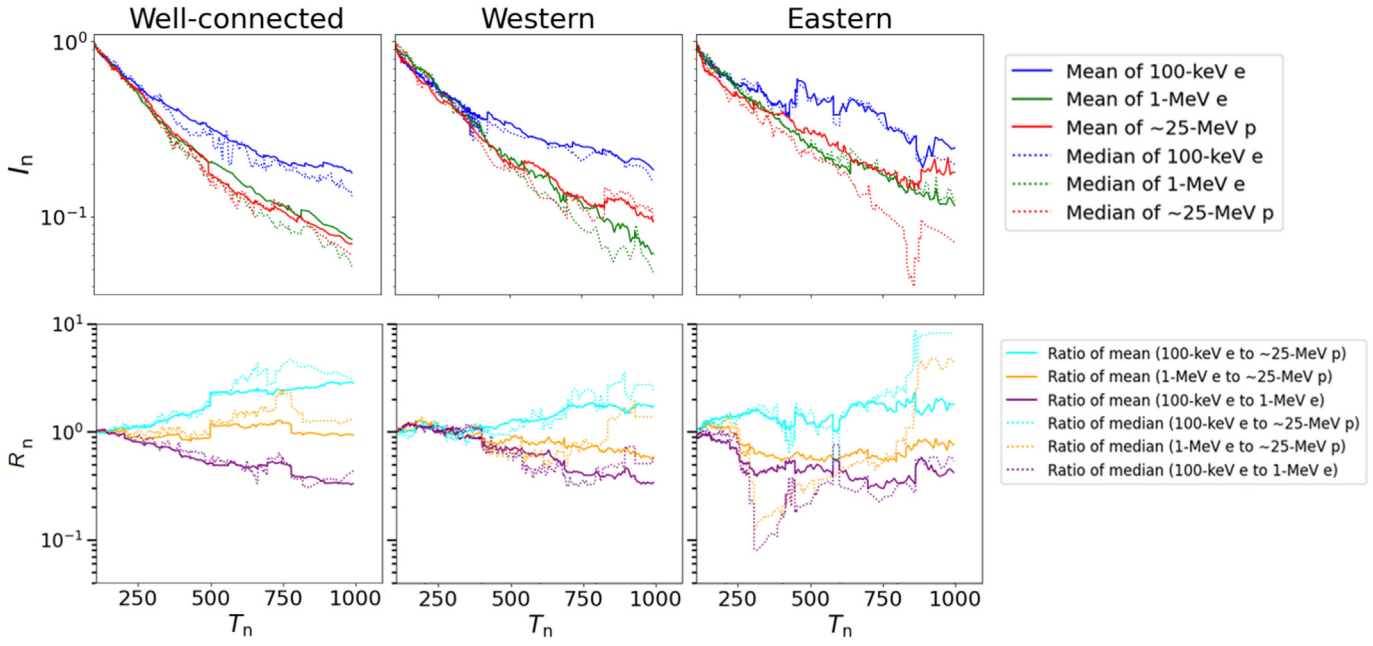

Fig. 6. The mean (solid curve) and median (dotted curve) (top panel) calculated for the decay phase of superposed profiles of SEP events observed for ~100-keV electrons (blue), ~1-MeV electrons (green), and ⩾ 25-MeV protons (red) for well-connected (left), western (middle), and eastern (right) events. The bottom panel shows the ratio R_n of the mean/ median (solid/ dotted curve) of the superposed normalized intensities for ~100-keV electrons to ⩾25-MeV protons (cyan), ~1-MeV electrons to ⩾25-MeV protons (orange), and ~1-MeV electrons to ~100-keV electrons (violet) for all three longitudinal sectors for the decay phase. (For interpretation of the references to colour in this figure legend, the reader is referred to the web version of this article.)

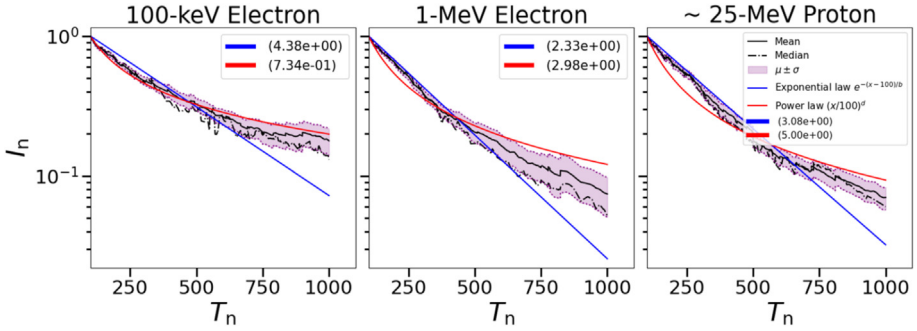

Fig. 7. An exponential (blue curve) and power (red curve) law fit applied on the mean (black solid curve) calculated for the decay phase of superposed profiles of SEP events observed for ~100-keV electrons (left), ~1-MeV electrons (middle), and ⩾25-MeV protons (right) for well-connected events. The purple-colored shaded region represents the uncertainty in the mean (μ) calculated as $\mu \pm \sigma$, where σ is the standard error of the mean. The value of the reduced chi-square calculated for both exponential (blue) and power (red) law fits is listed in the legend in the corresponding color. (For interpretation of the references to colour in this figure legend, the reader is referred to the web version of this article.)

$T_n = a$, maximize at $T_n = 100$, and have a unit value at the maximum,

$$f(T_n) = \left(\frac{100-a}{T_n-a}\right)^{c} \exp\left\{c\left(1-\frac{100-a}{T_n-a}\right)\right\}. \quad (1)$$

Wang et al. (2022) studied the propagation of energetic protons and reported the quantitative relation between the intensity-time profiles and helio-longitude of the observer. Using the solution of the diffusive transport equation, Wang et al. (2022) fitted the profile of ~50 MeV energetic proton events with an analytical function of the form $f(t) = a(t-t_0)^{-c} \exp\{-1/[b(t-t_0)]\}$ where a, c, b, and t_0 are fitting parameters and the onset time, respectively. Wang et al. (2022) concluded that the location of the observer, along with the SEP transport conditions, plays an important role in characterizing the shape of intensity profiles of SEPs.

Kahler and Ling (2017) fitted the time-intensity profiles of 14 large (E > 10 MeV) SEP proton events from the solar cycle 24 with a modified Weibull function $f(t) = (-\alpha/\beta)(t/\beta)^{\alpha-1} \exp\{-(t/\beta)^{\alpha}\}$ where α and β are the shaping and scaling parameters, respectively. Kahler and Ling (2017) studied the variation in the shapes of fitted profiles with the fitting parameters and concluded that

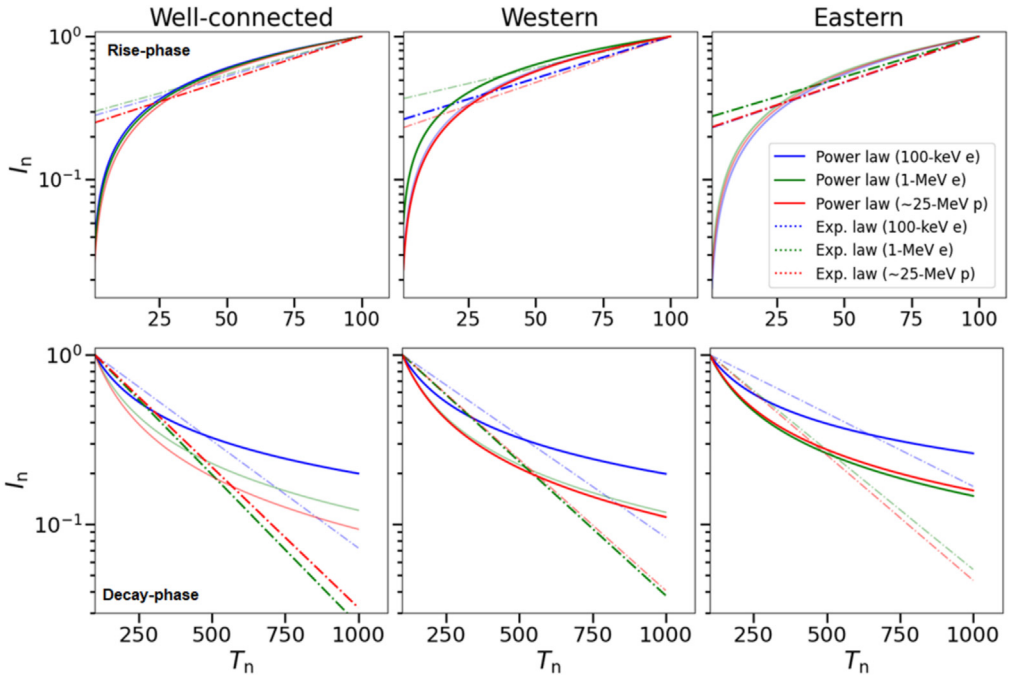

Fig. 8. Comparison of fits of two empirical models, exponential (dashed-dotted curve) and power law (solid curve) functions applied to the mean calculated for the superposed normalized profiles of SEP events, for the rise (top panel) and decay (bottom panel) phases. Results for ~100-keV electrons (blue), ~1-MeV electrons (green), and ⩾25-MeV protons (red) are shown for the well-connected (left), the poorly-connected western (middle), and the poorly-connected eastern (right) events. The brighter and thicker curves represent the better fit with the lower value of reduced chi-square for each panel. (For interpretation of the references to colour in this figure legend, the reader is referred to the web version of this article.)

these parameters provide significant measures of the shape and duration of the SEP event profiles that can be used for space weather applications.

The results of the present study are also compared with a Weibull model, which we obtained based on the function of Kahler and Ling (2017) by requiring the profile to start at $T_n = m$, maximize at $T_n = 100$, and have a unit value at the maximum intensity,

$$f(T_n) = \left(\frac{T_n + m}{100 + m}\right)^{l-1} \exp\left[\frac{l-1}{l}\left\{1 - \left(\frac{T_n + m}{100 + m}\right)^{l}\right\}\right] \quad (2)$$

It is clear from the summarized results in Fig. 9 that the mean behavior of normalized intensity profiles of both electron energies and ⩾25-MeV protons is rather similar, as well as for any of the well-connected or poorly-connected events. The exponential (blue) and power (red) law fits represent the mean behavior, in general, better, for the rise and the decay phases of all SEP events, respectively. The mean behavior is also in good agreement for the decay phase with both of the reference models (Wang et al., 2022, green) (Kahler and Ling, 2017, orange) while for the rise phase, the reference models do not perform well.

We also investigated the effect of different heliocentric locations of the observing spacecraft on the mean SEP profiles, but we do not find any significant difference for different locations (see C).

Farwa et al. (2025) analyzed the same sample of 45 multi-spacecraft SEP events used for the present study and proposed that six well-connected SEP events of the sample are flare-dominated while the rest of the events were suggested to be dominated by shock acceleration. We studied the shape of normalized intensity profiles and superposed epoch analysis parameters (Fig. 10) of the six well-connected SEP events proposed to be flare-dominated in comparison with the rest of the shock-dominated events. Fig. 10 compares the superposed normalized profiles (left column) and superposed epoch analysis parameters calculated for the rise (middle column) and the decay (right column) phase, showing the six flare-dominated events in green. The results for ~100-keV electrons, ~1-MeV electrons, and ⩾25-MeV protons are shown in the top, center, and bottom rows, respectively. All symbolic conventions are the same as in Figs. 2 and 5.

We note that for ~1-MeV electrons (central row), only three flare-dominated events are left after excluding the SOHO/EPHIN observations due to the contamination effects from the data set used for the present analysis. We find that the flare-dominated events show intensity profiles similar to the shock-associated events (Fig. 10, left), and there is no noticeable difference in the shapes of the flare-dominated profiles. Similarly, the mean (solid) and median (dashed-dotted) curves follow similar trends for both flare-dominated (green/lime) and shock-dominated events (black/gray) for both the rise (middle) and the decay (right) phases.

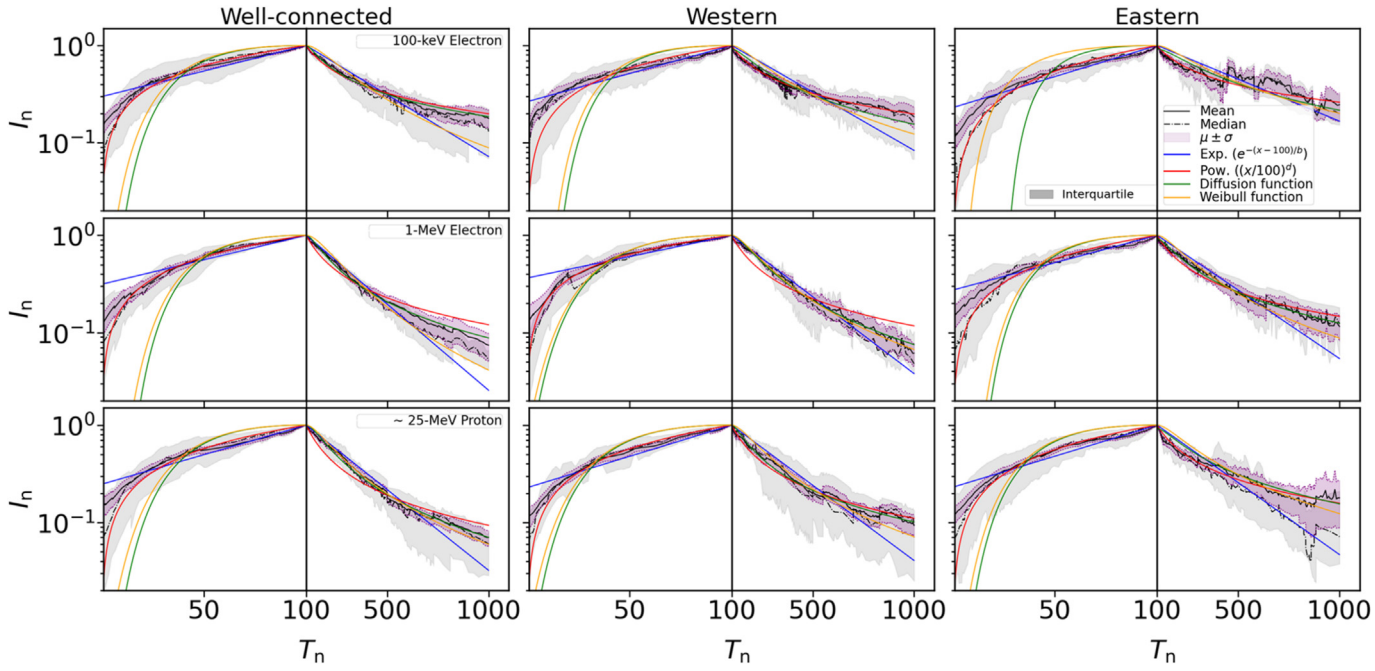

Fig. 9. Summary of the superposed epoch analysis results including the fits of the two empirical models, exponential (blue curve) and power law (red curve) functions, and the two reference models (green and orange curves, see text) applied to the mean (black solid curve), calculated for the superposed normalized profiles of the SEP events. Results for ~100-keV electrons (top), ~1-MeV electrons (center), and ⩾25-MeV protons (bottom) are shown for well-connected (left), poorly-connected western (middle), and poorly-connected eastern (right) events. The x-axis along 0 − 100, and 100 − 1000 represents the rise and the decay phase, respectively. Black (dash-dotted) colored curves and the purple shaded areas represent the median and the uncertainty calculated in the mean, respectively, and the inter-quartile region is shaded in gray. (For interpretation of the references to colour in this figure legend, the reader is referred to the web version of this article.)

3.3. Onset delays

Fig. 11 represents the distribution of onset delays between ⩾25-MeV protons and relativistic ~1-MeV electrons. In Fig. 11, we only considered events for which an onset delay uncertainty of ≤ 20 minutes was reported in the SERPENTINE catalog. Note that the data used for the calculation of onset delays is taken directly from the SERPENTINE SEP event catalog. As explained in Section 2, the spacecraft observations of the sample are taken at different heliocentric distances. We, therefore, applied radial scaling, shifting all spacecraft observations along the nominal Parker spiral to 1 au. We find that the first arriving particles, creating the onset of the events, mostly show a later arrival of ⩾25-MeV protons compared to ~1-MeV electrons, which is, in most cases, larger than 25 min/au, a reference onset delay, which would be expected, if both were injected at the same time. We note that six events have exceptionally short onset delays of ≤ 25 min/au (Fig. 11, first three bins). Among these six short onset delays, three events show ambiguity, which is potentially related to the longer time averaging used to determine the onset times, or due to uncertainty in the measurement of onset times, in case of data gaps in the onset region. In contrast, the other three events clearly reveal a short onset delay between electrons and protons. The mean onset delay is 70 min/au, and the median is 37 min/au. These results support the idea of using the earlier arrival of relativistic electrons as an alert for the later-arriving protons, which constitute the main radiation hazards. The Relativistic Electron Alert System for Exploration (REleASE) forecasting scheme (Posner, 2007) uses this effect to predict proton fluxes by utilizing the measured electron flux. This scheme depends on the high correlation between electrons and protons within a single event and makes the indirect assumption of a common acceleration process. In 15 out of the 45 multi-spacecraft SEP events of the used sample, both ~1-MeV electrons and ⩾25-MeV protons show similar longitudinal spreads and are observed by the same set of spacecraft. Considering the event sample in terms of single-spacecraft observations, we find 86 events in which both ~1-MeV electrons and ⩾25-MeV protons are observed. In seven (24) single-spacecraft events, only ~1-MeV electrons (⩾25-MeV protons) are observed.

As is obvious from Fig. 11, a few events show significantly smaller onset delays, which would pose a challenge to the REleASE system. We furthermore investigated the performance of REleASE for the six presumably flare-dominated SEP events reported by Farwa et al. (2025). For this purpose, we looked up the REleASE forecast results, available athttps://hesperia.astro.noa.gr/data-retrieval-tool/, which uses real-time electron observations from SOHO/COSTEP and ACE/EPAM to forecast proton flux. Using ACE/EPAM results we found that out of these six electron-rich events, one event is correctly forecasted to stay below the alarm threshold, one event was a miss, two

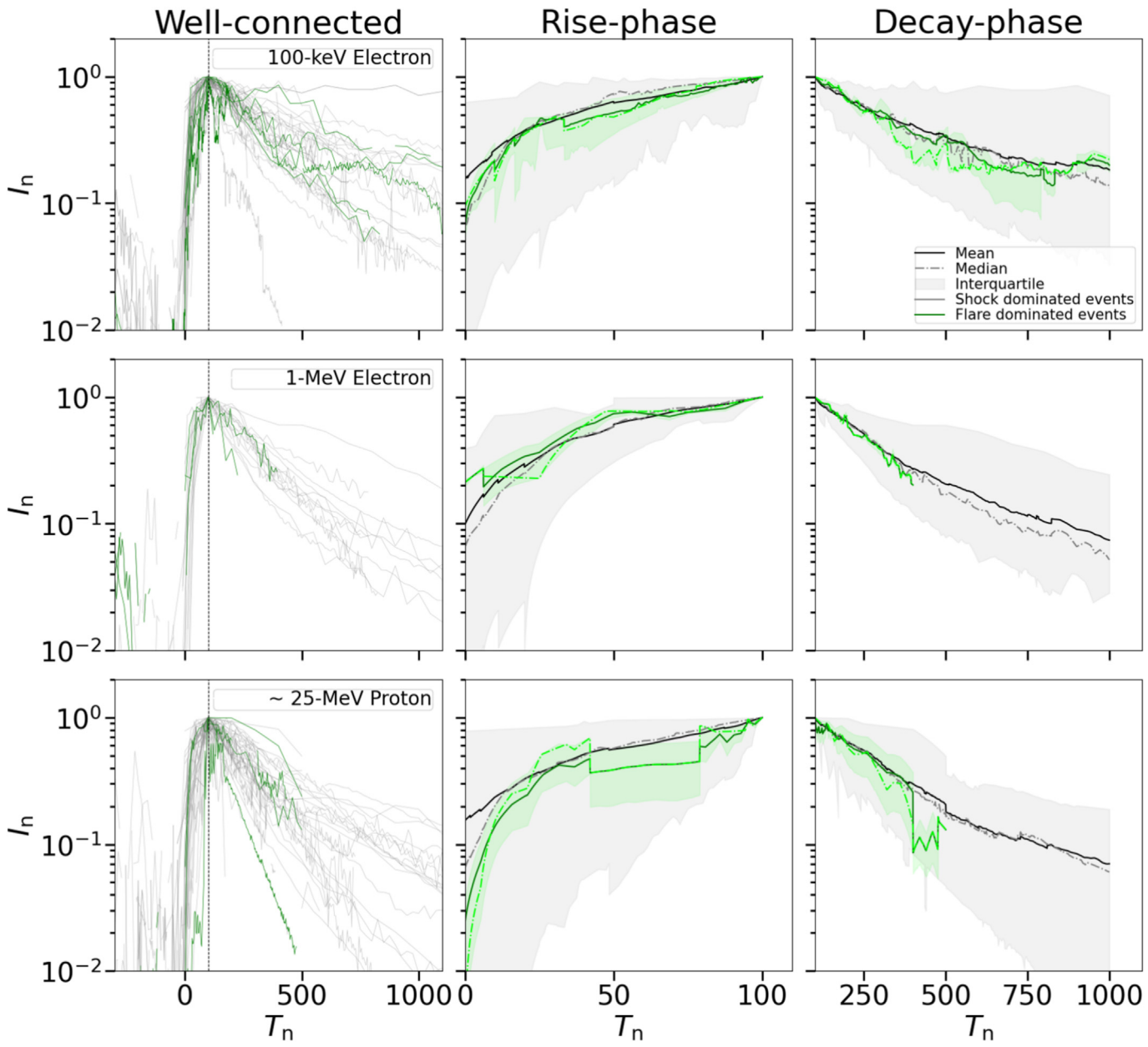

Fig. 10. The normalized profiles (left panel) and superposed epoch analysis parameters calculated for the rise (middle panel) and the decay (right panel) phase of flare-dominated (green/lime) SEP events in comparison to the rest of the observed (black/gray) SEP events for only the well-connected events for ~100-keV electrons (top panel), ~1-MeV electrons (center panel) and $\geqslant$ 25-MeV protons (bottom panel). The green/lime and black/gray colored curves represent the intensity profiles (left panel) and superposed epoch analysis parameters (middle, right panel) calculated for the six "flare-dominated" and the rest of the "shock-dominated" SEP events, respectively. The shaded lime and gray colored regions (middle, right panel) represent the inter-quartile region for the six "flare-dominated" and the rest of the shock-dominated SEP events, respectively. The solid and dashed-dotted curves (middle, right panel) represent the mean and the median, respectively. Note that for ~1-MeV electrons (central row), there are only three flare-dominated events left after excluding the SOHO/EPHIN observations due to contamination effects from the data set used for the present analysis. (For interpretation of the references to colour in this figure legend, the reader is referred to the web version of this article.)

events caused a false alarm, and for another two events the forecasted intensities were too high, stayed however below the alarm threshold. Counting only the real false-alarm cases yields a false alarm rate (FAR) of 33%, which is in agreement with the FAR reported as 35% for ACE/EPAM (Núñez et al., 2018).

4. Discussion

In this work, we analyzed a sample of 45 independent SEP events observed with a fleet of five spacecraft, resulting in 60–110 single spacecraft observations, depending on the particle species and energy. We performed a superposed

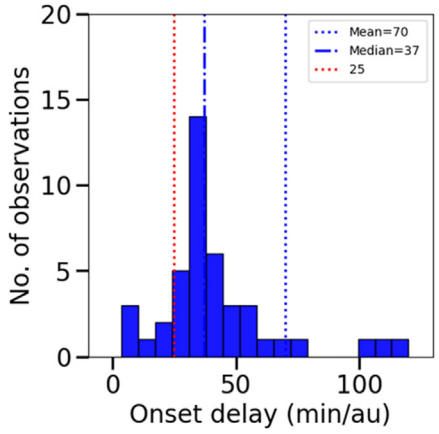

Fig. 11. The distribution of radially scaled onset delay time between the ⩾ 25-MeV protons and relativistic ∼1-MeV electrons. The blue dotted and dotted-dashed lines represent the mean and the median of the distribution, respectively. The red dotted line represents the onset delay of 25 min/au for a reference. (For interpretation of the references to colour in this figure legend, the reader is referred to the web version of this article.)

epoch analysis on the normalized intensity-time profiles for ∼100-keV electrons, ∼1-MeV electrons, and ⩾25-MeV protons, dividing the observations into well-connected and poorly-connected western and poorly-connected eastern events. The shapes of the resulting mean and median curves and empirical exponential and power law models applied to the mean curves are examined and compared for the electrons and protons for different longitudinal sectors.

There are some basic uncertainties in the methodology of the superposed epoch analysis applied to normalized intensity profiles. Depending on the contrast level between peak and background intensity for different events, using the background-subtracted intensities may result in different peak-to-background ratios, affecting the initial rise phase of some events. As described in Section 2, we have excluded the SEP profiles having successive bursts of solar activity that could produce mixing events and wide data gaps, leaving a sample of 60–110 single spacecraft observations for electrons and protons. As these profiles are further divided into the three longitudinal sectors (well-connected and poorly-connected western and eastern), this sometimes results in relatively small sample sizes for the superposed epoch analysis. Hence, limited statistics of the sample, mostly in the eastern sector, may have affected the accuracy of the results. We note that in the present study, we have excluded some single spacecraft observations for ∼100-keV electrons and all SOHO/EPHIN observations for ∼1-MeV electrons due to potential ion contamination effects.

Although the shapes of the mean and median profiles for each particle species appear quite similar in all longitudinal sectors, the individual inter-quartile bands are still quite broad, implying that there are still a lot of event-to-event variations for each particle species.

As shown in Fig. 1, we find a large event-to-event variation in the rise times and decay profiles with a variety of short-lived up to rather long-lived profiles. Especially large differences are found for the poorly-connected eastern events with several comparatively fast-decaying profiles. The well-connected and the poorly-connected western events have quite similar profiles, with the exception that the well-connected ∼100-keV electron profiles rather resemble the poorly-connected eastern ⩾25-MeV proton profiles.

For both the rise and the decay profiles, neither exponential nor power laws always represent the mean behavior better than the other. Often, the mean curves lie between these two models.

The similarity found in mean rise and decay profiles for electrons and protons may hint at similar acceleration mechanisms and source size. However, species- and energy-dependent transport effects may also be involved. The rather similar mean rise profiles found for electrons and protons are quite interesting from the space weather forecasting perspective. The similarity of the rise profiles and the onset delay between protons and relativistic electrons found by our study provides further support for the use of solar electron measurements to predict protons, which is already employed, e.g., in the REleASE forecasting scheme (Posner, 2007). We compared the superposed epoch analysis parameters for the six flare-dominated and the rest of the shock-dominated events as identified by Farwa et al. (2025) and noticed that the normalized intensity profiles, the mean, and the median curves follow similar trends for both flare-dominated and shock-dominated events for both the rise and the decay phases (Fig. 10). The absence of differences in the superposed epoch analysis results of flare-dominated and shock-dominated events suggests that superposed epoch analysis alone is not a sufficient tool to identify the potential flare and shock contribution to the SEP events.

Furthermore, the similarity in the average rise profile of relativistic electrons and ⩾25-MeV protons provides another possibility for space weather forecasting applications. The normalized intensity-time profiles could be used to generate an empirical model of proton fluxes to predict the peak time and peak intensity. Such a probabilistic model for peak intensities and rise times is proposed by (Papaioannou et al., 2022). As an attempt to understand the average SEP intensity profile, our studies are expected to contribute to improving space-weather forecasting applications.

5. Conclusions

In summary, we find that a sample of large SEP events, even exhibiting a mixture of impulsive and gradual profiles, can be reasonably represented by an average profile based on normalized time and intensity. Using the superposed epoch analysis, we find that the mean SEP profiles for electrons and protons are quite similar, supporting the concept of an advanced alert for energetic protons based on the earlier arrival of relativistic electrons. The limited sample size

in our study, however, calls for future analyses with extended datasets that will be measured as the solar cycle 25 progresses.

Declaration of competing interest

The authors declare that they have no known competing financial interests or personal relationships that could have appeared to influence the work reported in this paper.

Acknowledgments

This study is performed in the framework of the Finnish Centre of Excellence in Research of Sustainable Space (FORESAIL, Research Council of Finland grant 352847). We acknowledge funding by the European Union's Horizon Europe research and innovation program under grant agreement No. 101134999 (SOLER). The paper reflects only the authors' view, and the European Commission is not responsible for any use that may be made of the information it contains. N.D. and L.V. are grateful for support from the Research Council of Finland (SHOCKSEE, Grant No. 346902). L.V. acknowledges the financial support of the University of Turku Graduate School.

Appendix A. Parameters of empirical model

We fit the mean intensity profiles with different fitting functions and use the reduced chi-square to determine the best fit. The reduced chi-square χ^2_{red} and the chi-square χ^2 values are calculated as $\chi^2_{\text{red}} = \chi^2/\nu$ and $\chi^2 = \sum_{i=1}^{N}(R_i/\sigma_i)^2$, respectively. Here, ν is the degrees of freedom ($\nu = N - N_{\text{vars}}$, where N is the number of data points to fit and N_{vars} is the number of variables in the fitting function). R_i is the residual between the i-th mean intensity point and the model, and σ_i is the standard error of this i-th mean.

The reduced chi-square values and fit parameters are calculated for all four empirical models, i.e., exponential law, power law, the diffusion model based on the Wang et al. (2022) diffusion function, and the Weibull model based on the Kahler and Ling (2017) Weibull function for comparison.

Table A.2 summarizes fit parameters, the percentage error in the value of the fit parameter, and the reduced chi-square values calculated for all four empirical models applied to the mean curves calculated from the superposed epoch analysis of the normalized intensity profiles of ~100-keV electrons, ~1-MeV electrons, and ⩾25-MeV protons for well-connected and poorly-connected western and poorly-connected eastern events, both for the rise and the decay phases. The lower value of reduced chi-square, among exponential and power law fits, is highlighted in boldface, representing the better fit among these two models.

Appendix B. Including ~1-MeV electron SOHO/EPHIN data in the analysis

For ~1-MeV electrons all SOHO/EPHIN observations were excluded from the data set due to potential contamination effects. Fig. B.12 shows how the final results change if the data set is not excluded. The mean (solid curve), median (dotted curve), and the inter-quartiles calculated from the superposed epoch analysis for ~1-MeV electrons are presented for the rise (right column) and the decay phase (left column). The blue and red color scheme represents the results, including and excluding the SOHO/EPHIN observations, respectively. The shaded region represents the uncertainty in the mean (μ) calculated as $\mu \pm \sigma$, where σ is the standard error of the mean. We find that there is no significant difference in the superposed epoch analysis results calculated with or without SOHO/EPHIN observations. In both cases, the means agree within the error range, implying that the SOHO/EPHIN observations do not suffer from strong contamination effects.

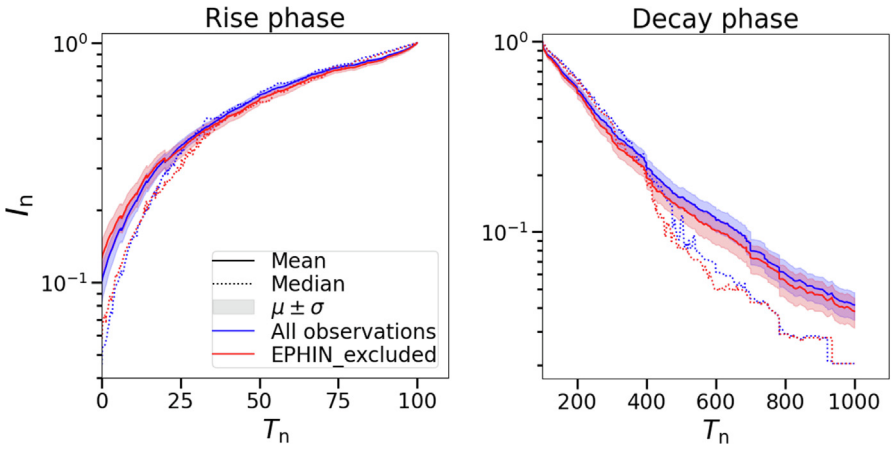

Fig. B.12. The mean (solid curve) and median (dotted curve) calculated for the rise (right) and decay (left) phase of superposed normalized profiles of SEP events observed for ~1-MeV electrons. The blue and red color schemes represent the results, including and excluding the ~1-MeV electrons of SOHO/EPHIN. The shaded regions represent the uncertainties in the mean (μ) calculated as $\mu \pm \sigma$, where σ is the standard error of the mean.

Appendix C. Influence of heliocentric distances

The observing spacecraft of the sample are located at different heliocentric locations, with the heliocentric distance r varying from 0.07 to 1.01 au. To investigate a potential effect of the variation in r on the shapes of the mean and median profiles of electrons and protons, we compare the mean (median) profiles (Fig. C.13) among all values of r (blue) with a subset of the sample with $r \leqslant 0.6$ au (red) for both the rise (Fig. C.13, top panel) and the decay phase (Fig. C.13, bottom panel). It is clear from Fig. C.13 that the mean profiles for all particle species do not differ significantly based on the two different samples.

Appendix D. Variation of normalization parameters

As described in Section 2.1, the intensity is normalized to the peak intensity I_{peak} and the time is normalized to the rise time of the SEP event. To investigate the variations of the time normalization parameter, we show the relationship between the rise times of ~100-keV electrons, ~1-MeV electrons, and $\geqslant$ 25-MeV protons for all SEP events in Fig. D.14, which summarizes the parameters over all

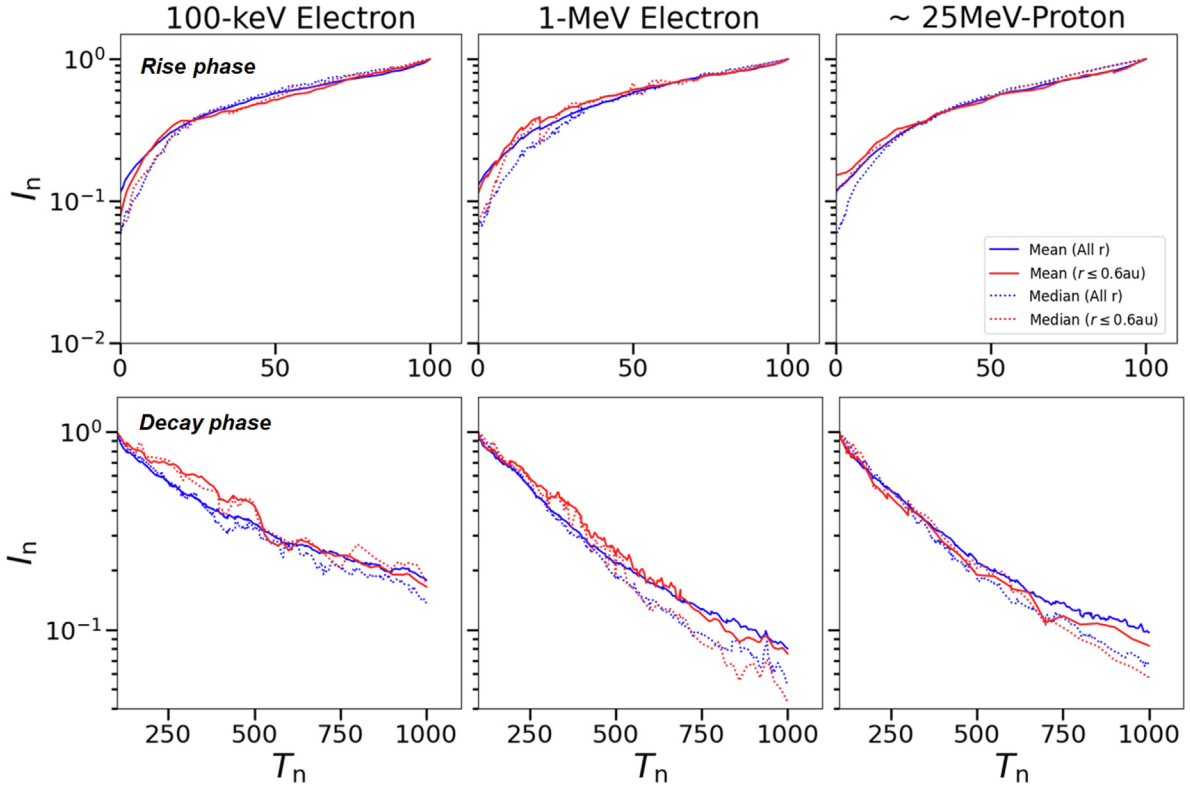

Fig. C.13. The mean (solid curve) and the median (dotted curve) intensities, calculated for the rise (top panel) and the decay (bottom panel) phase of superposed normalized profiles of SEP events observed for ~100-keV electrons (left), ~1-MeV electrons (middle), and $\geqslant$ 25-MeV protons (right) for all values of heliocentric distances r (blue) and for the values $r \leqslant 0.6$ au (red). (For interpretation of the references to colour in this figure legend, the reader is referred to the web version of this article.)

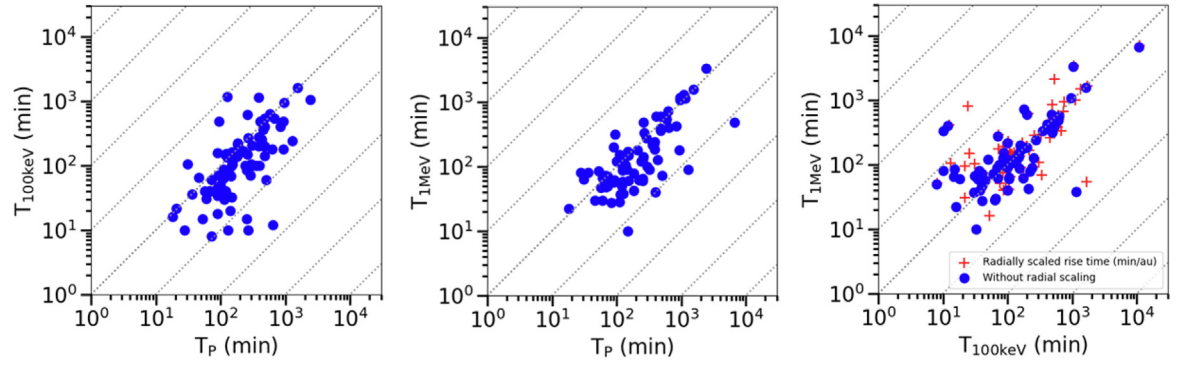

Fig. D.14. The time normalization parameters for ~100-keV electrons (left), and ~1-MeV electrons (middle) as a function of $\geqslant$ 25-MeV protons. The right panel shows the time normalization parameters for ~1-MeV electrons as a function of ~100-keV electrons. The red crosses show the same parameters but with radial scaling being applied. (For interpretation of the references to colour in this figure legend, the reader is referred to the web version of this article.)

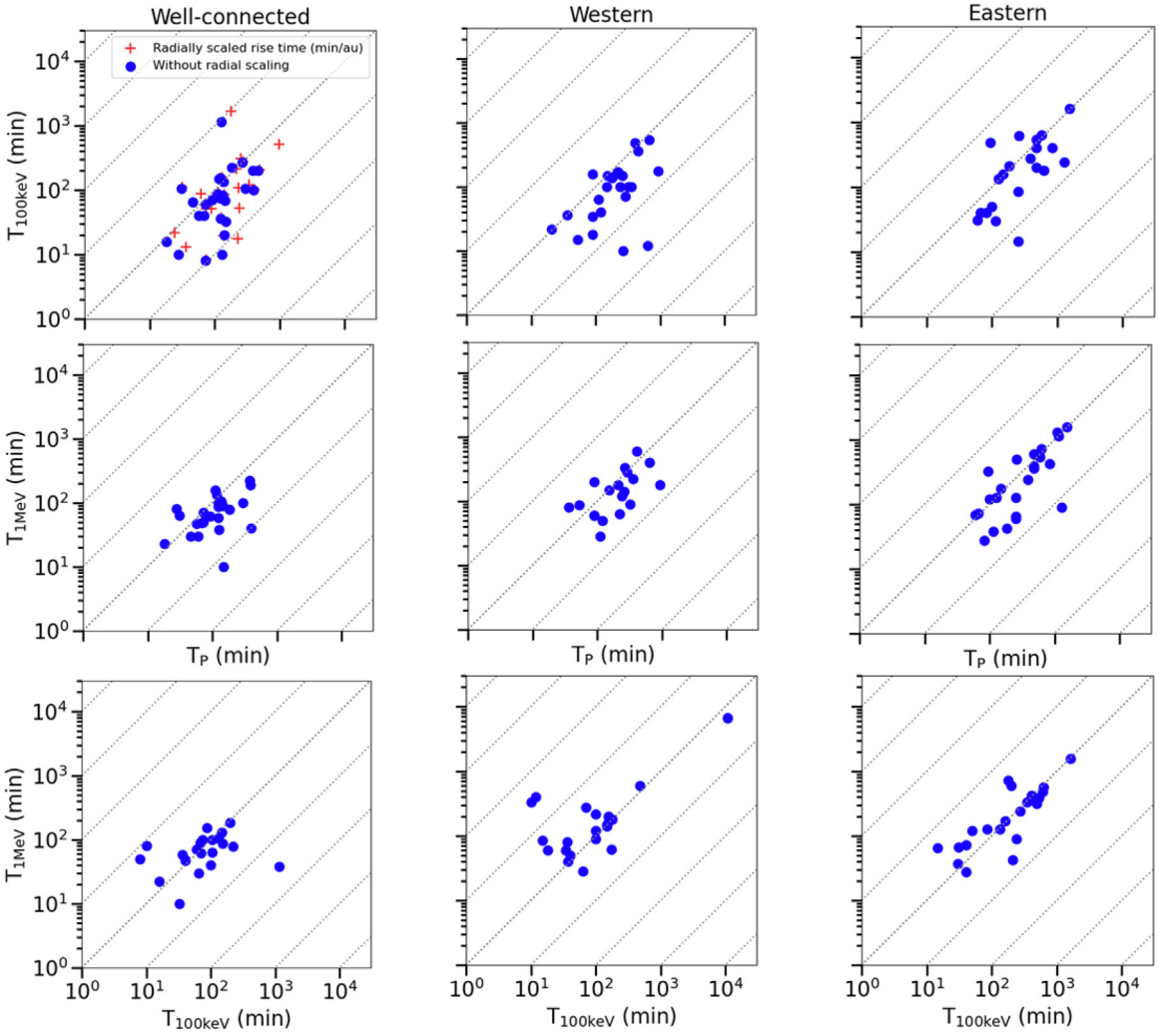

Fig. D.15. Same as Fig. D.14 but broken down for the three longitudinal sectors. The red and blue symbols (top left panel) represent the results with and without radial scaling, respectively, applied to the measurements of the time normaliz.ation parameter.

three longitudinal sectors. Fig. D.14 (left) also includes the radially scaled values (red crosses), which do, however, not show an effect on the variation of time normalization parameters. Fig. D.15) shows the same parameters broken down into the three longitudinal sectors. Although some amount of scattering is present, the plots show an overall one-to-one dependence (dashed lines guide the eye) of the parameters. The variation of the intensity normalization parameters, I_{peak}, has been studied and presented by Farwa et al. (2025).

References

Beck, P., Latocha, M., Rollet, S. et al., 2005. Tepc reference measurements at aircraft altitudes during a solar storm. Adv. Space Res., 36(9), 1627–1633.https://www.sciencedirect.com/science/article/pii/S0273117705005946. doi: 10.1016/j.asr.2005.05.035. Space Life Sciences: Aircraft and Space Radiation Environment.

Benkhoff, J., Murakami, G., Baumjohann, W., et al., 2021. BepiColombo - mission overview and science goals. Space Sci. Rev. 217 (8), 90. https://doi.org/10.1007/s11214-021-00861-4.

Cane, H.V., 1985. The evolution of interplanetary shocks. J. Geophys. Res.: Space Phys. 90 (A1), 191–197. https://doi.org/10.1029/JA090iA01p00191.

Cane, H.V., Reames, D.V., von Rosenvinge, T.T., 1988. The role of interplanetary shocks in the longitude distribution of solar energetic particles. J. Geophys. Res. 93 (A9), 9555–9567. https://doi.org/10.1029/JA093iA09p09555.

Domingo, V., Fleck, B., Poland, A.I., 1995. The SOHO mission: an overview. Sol. Phys. 162 (1–2), 1–37. https://doi.org/10.1007/BF00733425.

Dresing, N., Gómez-Herrero, R., Heber, B., et al., 2014. Statistical survey of widely spread out solar electron events observed with STEREO and ACE with special attention to anisotropies. Astron. Astrophys. 567, A27. https://doi.org/10.1051/0004-6361/201423789.

Dresing, N., Yli-Laurila, A., Valkila, S., et al., 2024. The solar cycle 25 multi-spacecraft solar energetic particle event catalog of the SERPENTINE project. Astron. Astrophys. 687, A72. https://doi.org/10.1051/0004-6361/202449831, arXiv:2403.00658.

Farwa, G.U., Dresing, N., Gieseler, J., et al., 2025. Electron and proton peak intensities as observed by a five-spacecraft fleet in solar cycle 25. Astron. Astrophys. 693, A198. https://doi.org/10.1051/0004-6361/202450945.

Fiori, R.A.D., Kumar, V.V., Boteler, D.H., et al., 2022. Occurrence rate and duration of space weather impacts on high-frequency radio

communication used by aviation. J. Space Weather Space Clim. 12, 21. https://doi.org/10.1051/swsc/2022017.

Fox, N.J., Velli, M.C., Bale, S.D., et al., 2016. The solar probe plus mission: humanity's first visit to our star. Space Sci. Rev. 204 (1–4), 7–48. https://doi.org/10.1007/s11214-015-0211-6.

Getley, I.L., Duldig, M.L., Smart, D.F., et al., 2005. Radiation dose along North American transcontinental flight paths during quiescent and disturbed geomagnetic conditions. Space Weather 3 (1), S01004. https://doi.org/10.1029/2004SW000110.

Gieseler, J., Dresing, N., Palmroos, C., et al., 2023. Solar-MACH: An open-source tool to analyze solar magnetic connection configurations. Front. Astron. Space Sci. 9, 384. https://doi.org/10.3389/fspas.2022.1058810, arXiv:2210.00819.

Haggerty, D.K., Roelof, E.C., 2002. Impulsive near-relativistic solar electron events: delayed injection with respect to solar electromagnetic emission. Astrophys. J. 579, 841–853. https://doi.org/10.1086/342870.

Haggerty, D.K., Roelof, E.C., Simnett, G.M., 2003. Escaping near-relativistic electron beams from the solar corona. Adv. Space Res. 32 (12), 2673–2678. https://doi.org/10.1016/S0273-1177(03)00929-3.

Iucci, N., Levitin, A.E., Belov, A.V., et al., 2005. Space weather conditions and spacecraft anomalies in different orbits. Space Weather 3 (1), 01001. https://doi.org/10.1029/2003SW000056.

Kahler, S.W., Ling, A.G., 2017. Characterizing solar energetic particle event profiles with two-parameter fits. Sol. Phys. 292 (4), 59. https://doi.org/10.1007/s11207-017-1085-4.

Kaiser, M.L., Kucera, T.A., Davila, J.M., et al., 2008. The STEREO mission: an introduction. Space Sci. Rev. 136 (1–4), 5–16. https://doi.org/10.1007/s11214-007-9277-0.

Kartavykh, Y., Rodríguez-García, L., Heber, B., et al., 2025. A statistical study of energetic particle events associated with interplanetary shocks observed by Solar Orbiter in solar cycle 25. A&A 699, A24. https://doi.org/10.1051/0004-6361/202553775.

Kecskeméty, K., Daibog, E.I., Logachev, Y.I., et al., 2009. The decay phase of solar energetic particle events. J. Geophys. Res. (Space Phys.) 114 (A6), A06102. https://doi.org/10.1029/2008JA013730.

Krucker, S., Kontar, E.P., Christe, S. et al., 2007. Solar flare electron spectra at the Sun and near the Earth. Astrophys. J., 663, L109–L112. http://adsabs.harvard.edu/abs/2007ApJ...663L.109K. doi:10.1086/519373.

Lario, D., 2010. Statistical study on the decay phase of solar near-relativistic electron events. Astrophys. J. Suppl. Ser. 189 (1), 181. https://doi.org/10.1088/0067-0049/189/1/181.

Lario, D., Aran, A., Gómez-Herrero, R., et al., 2013. Longitudinal and radial dependence of solar energetic particle peak intensities: STEREO, ACE, SOHO, GOES, and MESSENGER observations. Astrophys. J. 767, 41. https://doi.org/10.1088/0004-637X/767/1/41.

Müller, D., St. Cyr, O.C., Zouganelis, I., et al., 2020. The solar orbiter mission. Science overview. Astron. Astrophys. 642, A1. https://doi.org/10.1051/0004-6361/202038467, arXiv:2009.00861.

Núñez, M., Klein, K.-L., Heber, B., et al., 2018. Hesperia forecasting tools: Real-time and post-event. In: Malandraki, O.E., Crosby, N.B. (Eds.), Solar Particle Radiation Storms Forecasting and Analysis: The HESPERIA HORIZON 2020 Project and Beyond. Springer International Publishing, Cham, pp. 113–131. https://doi.org/10.1007/978-3-319-60051-2_7.

Ogilvie, K.W., Desch, M.D., 1997. The wind spacecraft and its early scientific results. Adv. Space Res. 20 (4–5), 559–568. https://doi.org/10.1016/S0273-1177(97)00439-0.

Papaioannou, A., Vainio, R., Raukunen, O., et al., 2022. The probabilistic solar particle event forecasting (PROSPER) model. J. Space Weather Space Clim. 12, 24. https://doi.org/10.1051/swsc/2022019, arXiv:2205.07325.

Posner, A., 2007. Up to 1-hour forecasting of radiation hazards from solar energetic ion events with relativistic electrons. Space Weather 5 (5), 05001. https://doi.org/10.1029/2006SW000268.

Reames, D.V., 1999. Particle acceleration at the Sun and in the heliosphere. Space Sci. Rev. 90, 413–491, URL: http://adsabs.harvard.edu/abs/1999SSRv...90..413R.

Reames, D.V., 2015. What are the sources of solar energetic particles? Element abundances and source plasma temperatures. Space Sci. Rev. 194 (1), 303–327. https://doi.org/10.1007/s11214-015-0210-7.

Reames, D.V., Barbier, L.M., Ng, C.K., 1996. The spatial distribution of particles accelerated by coronal mass ejection–driven shocks. Astrophys. J. 466, 473. https://doi.org/10.1086/177525.

Richardson, I.G., von Rosenvinge, T.T., Cane, H.V., et al., 2014. >25 MeV proton events observed by the high energy telescopes on the STEREO A and B spacecraft and/or at Earth during the first ~ seven years of the STEREO Mission. Sol. Phys. 289, 3059–3107. https://doi.org/10.1007/s11207-014-0524-8.

Rodríguez-García, L., Gómez-Herrero, R., Dresing, N., et al., 2023. Solar energetic electron events measured by MESSENGER and Solar Orbiter. Peak intensity and energy spectrum radial dependences: statistical analysis. Astron. Astrophys. 670, A51. https://doi.org/10.1051/0004-6361/202244553, arXiv:2211.11054.

Vainio, R., Desorgher, L., Heynderickx, D., et al., 2009. Dynamics of the earth's particle radiation environment. Space Sci. Rev. 147 (3), 187–231. https://doi.org/10.1007/s11214-009-9496-7.

Wang, Y., Lyu, D., Qin, G., et al., 2021. The effects of magnetic boundary on the uniform distribution of energetic particle intensities observed by multiple spacecraft. Astrophys. J. 913 (1), 66. https://doi.org/10.3847/1538-4357/abf9a4.

Wang, Y., Lyu, D., Wu, X., et al., 2022. The quantitative relation of the time profiles of intensities in the well-connected solar energetic particle events. Astrophys. J. 940 (1), 67. https://doi.org/10.3847/1538-4357/ac99da.

Wilson, I., Lynn, B., Brosius, A.L., Gopalswamy, N., et al., 2021. A quarter century of wind spacecraft discoveries. Rev. Geophys. 59 (2). https://doi.org/10.1029/2020RG000714, e2020RG000714.

Wraase, S., Heber, B., Böttcher, S., et al., 2018. Interpretation of increased energetic particle flux measurements by SEPT aboard the STEREO spacecraft and contamination. Astron. Astrophys. 611, A100. https://doi.org/10.1051/0004-6361/201732063, arXiv:1801.01040.